Calibration of a resonance energy transfer imaging system

Michael Ludwig, Nancy F. Hensel, and Robert J. Hartzman
C. W. "Bill" Young Marrow Donor Recruitment and Research Program, Naval Medical Research Institute, Bethesda, Maryland 20889-5055; and Georgetown University School of Medicine, Department of Pediatrics, Washington, DC 20007 USA

ABSTRACT A quantitative technique for the nondestructive visualization of nanometer scale intermolecular separations in a living system is described. A calibration procedure for the acquisition and analysis of resonance energy transfer (RET) image data is outlined. The factors limiting RET imaging of biological samples are discussed. Measurements required for the calibration include: (*a*) the spectral sensitivity of the image intensifier (or camera); (*b*) the transmission spectra of the emission filters; and (*c*) the quantum distribution functions of the energy transfer pair measured in situ. Resonance energy transfer imaging is demonstrated for two DNA specific dyes. The Förster critical distance for energy transfer between Hoechst 33342 (HO) and acridine orange (AO) is 4.5 ± 0.7 nm. This distance is slightly greater than the distance of a single turn of the DNA helix (3.5 nm or ~10 base pairs), and is well below the optical diffraction limit. Timed sequences of intracellular energy transfer reveal nuclear structure, strikingly similar to that observed with confocal and electron microscopy, and may show the spatial distribution of eu- and hetero- chromatin in the interphase nuclei.

INTRODUCTION

Fluorescence labeling of macromolecules and organelles has become a standard technique for observing cellular structure (1–7). In this paper, we present the first quantitative measurements of nanometer scale spatial distribution of fluorescent probes in a living system. Resonance energy transfer (RET) occurs between two dyes if: (*a*) the dyes are in close proximity (typically, <10 nm) to each other; (*b*) there is overlap between the emission spectrum of the donor dye and the absorption spectrum of the acceptor dye; and (*c*) the relative orientation of the two dyes is such that at some time during the lifetime of the donor excited state, the vectors representing the transition dipoles of donor emission and acceptor absorption are not perpendicular (8–10). The occurrence of RET is measured by observing sensitized acceptor emission with concurrent quenching of donor fluorescence.

The calibrated acceptor/donor ratio images reveal dye interactions on a scale well below the 250-nm resolution of the diffraction limited images (3). Because the RET images are diffraction limited, the intensity ratio at each pixel represents the average of underlying RET. Quantitatively accurate measurements of average intermolecular distances require an assessment of the orientation of the energy transfer dye pair and measurements of in situ absorption and emission spectra.

The methods developed here for calibrating RET images are based on absorption, emission and polarization spectral measurements of the donor and acceptor dyes and on the optical properties of the microscope and the imaging apparatus. It is essential in RET measurements to avoid photobleaching and saturation effects caused by high incident powers. Emission depolarization measurements were used to determine limiting values for the RET orientation factor κ^2 (11, 12).

The calibration procedure is verified by comparing acceptor/donor intensity ratios in the images to the intensity ratios observed in a fluorometer. The images permit examination of individual cells and intracellular structure. RET between two DNA specific dyes, acridine orange (AO, energy acceptor) and Hoechst 33342 (HO, energy donor) was observed in aqueous DNA solutions and in human peripheral blood lymphocytes. HO specifically binds to the minor groove of β-DNA whereas AO intercalates between two base pairs (13, 14). To distinguish regions of varying density in the nuclei of live interphase cells, the cells were initially stained with HO. Acridine orange was then added to the medium and its accumulation was measured as a function of time. Nuclear regions of low density (euchromatin) are more accessible to the AO than the more dense heterochromatin, and hence are seen as regions of high acceptor/donor intensity ratio.

EXPERIMENTAL METHODS

Staining and sample preparation

Acridine Orange, (3, 6-Bis[dimethylamino]acridium chloride hemi [zinc chloride]), (MW 370 g/mol) was obtained from Sigma Chemical Company (St. Louis, MO). 30 mg AO was dissolved in 1.0 ml ethanol (13, 14). The ethanol solution was diluted to a final concentration of

4.82×10^{-4} M AO with phosphate buffered saline (PBS, pH 7.4) solution. 1.0 ml aliquots of this AO stock solution were frozen and stored at −80°C in the dark. Acridine orange is an intercalating agent that will also bind to single stranded RNA and proteins primarily through electrostatic forces (15). The fluorescence spectrum of AO/nucleic acid complexes depends on both the concentration of AO and the structure of the nucleic acid (13, 14, 16–18). AO intercalation causes a local unwinding of 10° in the DNA helix (19).

The bisbenzimide dye 33342 Hoechst (MW 615 g/mol) was obtained from Calbiochem (La Jolla, CA). A 3.25×10^{-5} M stock solution of HO in PBS was prepared. 1.0-ml aliquots of the stock solution were frozen and stored at −80°C in the dark. HO is a nonintercalating agent that specifically binds to A-T regions along the minor groove of double stranded β-DNA. HO specifically binds to the minor groove of β-DNA in solution, in isolated chromosomes, and in intact cells (20–23). The fluorescence quantum yield of HO increases at least fifty-fold when bound. HO does not bind to single stranded nucleic acids. Previous studies have shown the cytotoxic effects due to the accumulation of HO are not appreciable in the short incubation and observation times of these experiments (21–24).

Human peripheral blood lymphocytes (PBLs) were harvested from whole blood using the Ficoll Hypaque protocol (25). Lymphocytes were frozen and stored in liquid nitrogen. After rapid thawing and washing to remove debris and dimethyl sulfoxide, the cells were suspended in RPMI 1640 medium supplemented with 10% fetal calf serum. The viability of the thawed lymphocytes was 95–99%. 2.0-ml aliquots of 2.4×10^6 cells were stained by incubating them in medium containing 15.1 μM HO at 37° for 30 min. After incubation, the cells were washed three times with medium and resuspended in RPMI 1640 (without phenol red or fetal calf serum, 10^7 cells/ml).

For the spectral measurements of energy transfer, HO stained cells were incubated for an additional 30 min with medium containing AO. The fluorescence from 2.0 ml of cells suspended in PBS was measured. In the imaging experiments, 20 μl of the cell suspension was applied to Cell Tak (Collaborative Research, Bedford, MA) coated glass coverslips and incubated for an additional 10 min at 37°C. Cell Tak, an adhesive protein, was used to limit cell movement over the course of the experiments. The coverslip was gently rinsed with medium and was then placed over a block of plexiglass surrounding 60-μl basin. The volume between the coverslip and the plexiglass formed a flow-through chamber. Medium could be injected into the chamber using capillary channels drilled through the plexiglass. AO stock solutions diluted with PBS were delivered to the flow chamber to initiate the imaging experiments. The chamber remained filled with AO medium for the duration of each experiment. The experiment occurred at room temperature (uncontrolled) in the flow chamber.

Instrumentation

Fig. 1 shows the apparatus for sample excitation and imaging. A Tracor Northern (Middleton, WI) Fluoroplex III houses the xenon lamp and power supply (Xe). The lamp output illuminates a turning mirror (T) and a chopper wheel (C). Light incident on the chopper is either transmitted to monochromator 1 (M1) or reflected towards monochromator 2 (M2). Using this configuration, two excitation wavelengths may be delivered to either the fluorometer or the microscope in an alternating cycle. A fiber optic cable delivers the selected excitation frequencies to either a sample cuvette placed in a Tracor Northern 6500 fluorimeter (TN6500) or to the flow chamber mounted in an inverted microscope described above. 350 nm (bandwidth 10.6 nm FWHM) light was used for excitation of HO and 470 nm (11.6 nm FWHM) light was used for direct excitation of AO.

Epifluorescence illumination was used for the microscopic imaging. The fiber optic output was directed toward a dichroic beamsplitter operated at 45°. The dichroic reflected the 350-nm exciting light toward the microscope objective but transmitted longer wavelength light. The percent transmission of the dichroic was 86 to 92% for wavelengths between 450 and 550 nm. A Nikon 1.3 NA 100X oil immersion fluorescence objective focused the excitation light on the sample field and also collected the fluorescence light. The 1.3 NA objective determines the 250 nm diffraction limited resolution of these images (4). Bandpass filters supplied by Omega (Brattleboro, VT) were housed in a Ludl (Hawthorne, NY) electronically controlled filter wheel (F). The donor dye emission was observed with a bandpass filter centered at 470 nm with 15 nm half width (FWHM) and 75% maximum transmission. The acceptor dye emission was observed with a bandpass filter centered at 530 nm with 30 nm FWHM and 80% maximum transmission.

The microscope image was focused on a calibrated video scope (Video Scope Intl., Ltd., Washington, DC) KS-1381 image intensifier with adjustable gain (INT). The intensifier utilized a modified S-25 photocathode with enhanced blue green sensitivity. The spectral response of the intensifier ($S(\lambda)$ in Eqs. 3 and 4) was measured by comparing its response to the response of a calibrated Ealing Electro-Optics (Holliston, MA) 28-0925 research radiometer. The temporal resolution of the imaging system is limited by the response time of the image intensifier. The intensifier recovery time, the time required for the full restoration of an image after a rapid change in photocathode illuminance, is 0.5 s. A Cohu (San Diego, CA) 4810 Solid State CCD video camera was the pickup device of the intensifier output (VC). The images were collected at video rates (30 frames/s).

The analog video signal was digitized for display and analysis to 512×473 pixels in a Tracor Northern (Middleton, WI) 8500 (TN8500) image analysis system. The TN8500 was used to analyze, display, and store the digitized images. Shot noise from the low light level video camera was reduced by accumulating and averaging 30 digitized frames. Threshold values for particle intensity and particle size were used to construct image binaries and define measurement fields (26). (Image binaries are representation of grey value images used in many image processing operations. Only those pixels of the grey value image that are turned on in the image binaries are evaluated in the ensuing image analysis.) A 530-nm acceptor image was measured immediately after the measurement of a 470-nm acceptor image. Each 530-nm image was coupled to a 470-nm image to form an energy transfer image pair. A background dark current image, measured by closing a shutter between the camera and the light source, was subtracted from each image before dividing. A shading correction was not required because of the flat illumination field provided by Fluoroplex III and the small portion of the field sampled by the objective. Binary images were constructed for each image pair measured. The time required for recording an image pair, including the time required for changing the emission filter, was 4 s.

In the TN6500 fluorimeter, emission spectra are measured by dispersing the emitted light onto an intensified photodiode array detector (PDA). The spectral response of the TN6500 and the fiber optic output was measured by comparing its response to the response of a calibrated Ealing Electro-Optics 28-0925 research radiometer. Steady-state polarization measurements were made on cells stained with HO only, AO only, and with both dyes in an attempt to measure limiting values for the energy transfer orientation factor. The observed fluorescence intensities polarized in the same direction as ($I_\parallel$) and perpendicularly to ($I_\perp$) the incident excitation were observed. The emission anisotropy was calculated from the observed spectra (11, 12). The absorption spectra of the solutions and transmission spectra of the filters were measured with a Cary Model 219 double-beam spectrophotometer (Varion Techtron Pty, Ltd., Victoria, Australia).

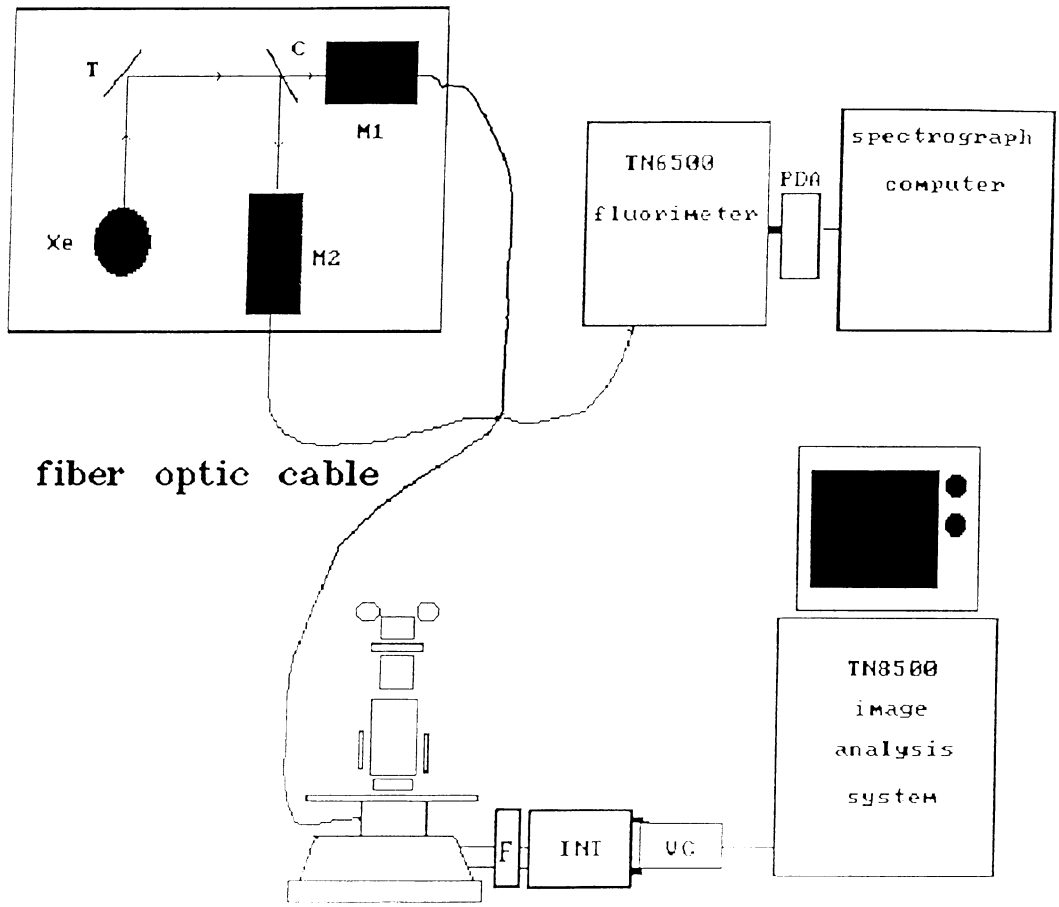

FIGURE 1 The Tracor Northern imaging system. The xenon lamp (Xe) illuminates a mirror (T) which in turn illuminates a chopper wheel (C). Light from the chopper is either transmitted toward one monochromator (M1) or reflected toward the other monochromator (M2). The output of the monochromators is fed into a fiber optic cable with two bundles. The fiber optic cable may be mounted to excite a sample in either a fluorometer with a photodiode array detector (PDA) or an inverted microscope. The microscope output passes through emission barrier filters (F) and illuminates an image intensifier (INT). A video camera picks up the intensifier output (VC). A Tracor Northern image analysis system is used for A/D conversion, image analysis, and display.

RESULTS

Measurements of in situ absorption and emission spectra of the energy transfer pair are required to evaluate RET imaging data. The local environment of a dye may significantly influence its absorption and fluorescence spectrum. For example, AO is a metachromatic dye; microenvironmental factors influence the bandwidth and maximum of its fluorescence spectrum. Hence, AO stains different tissues different colors. The spectra used in the RET proximity calculations must therefore be acquired in the in situ environment of the dye, or in an environment closely approximating it. Although the AO emission spectrum is not used in the calculation of the overlap integral (O in Eq. 2) it appears in the calculation of the image processing coefficients described below.

Fig. 2 shows the absorption and emission spectra of aqueous DNA complexes of HO and AO. The energy transfer studies were carried out with 350-nm excitation. At 350 nm, the molar extinction coefficient of AO is $<10\%$ that of HO. The purine and pyrimidine base pairs of DNA do not absorb in this spectral region, and do not directly interfere with energy transfer processes (27). Table 1 lists the absorption and emission spectral data for free HO and AO and their nucleic acid complexes.

The emission spectra of AO stained PBLs was measured as a function of AO concentration in the incubating medium to insure that the appropriate spectra were

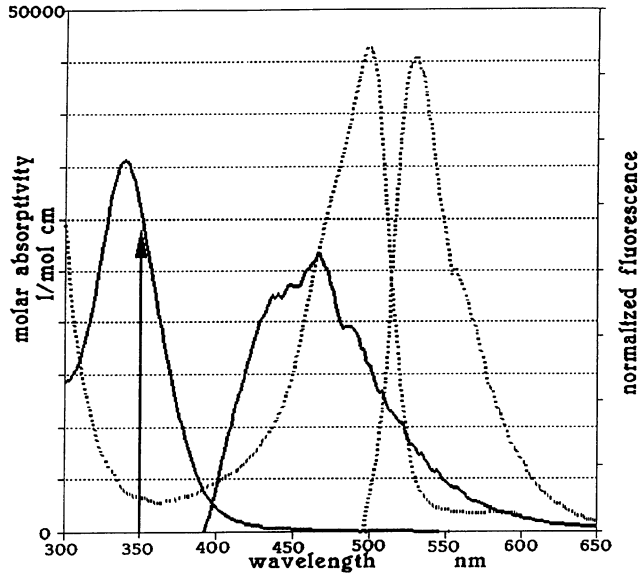

FIGURE 2 The absorption spectra and quantum distribution functions of HO (*solid line*) and AO (*dotted line*). The spectra were measured in DNA saturated aqueous solution with the following concentrations: 4.75 μM HO (absorption), 0.92 μM HO (emission), 5.4 μM AO (absorption), and 2.2 μM AO (emission). The absorption spectrum of AO shown here was used in the calculation of the energy transfer overlap integral in Eq. 2. The emission spectra shown here were not used either for the calculation of O or for the calculation of the image coefficients (Table 4). Instead, the emission spectra of stained PBLs were measured. See text for details.

used in the calculations of average intermolecular separation and to determine the effect of bound AO species formation on the observed AO intensity. The fluorescence spectra from populations of PBLs incubated in medium containing AO concentrations ranging from 0.32 to 4.82 μM are shown in Fig. 3. Each sample cuvette held 1.2×10^6 cells/ml. The upper limit of AO concentration for the cells incubated with 4.82 μM AO, assuming homogeneous uptake, is 4.0×10^{-15} mol/cell. The fluorescence spectral maximum occurred at 526 nm throughout the range of AO concentrations used.

Fig. 4 shows that the fluorescence intensity of both AO/aqueous DNA (*triangles*) and PBLs (*rectangles*) is linear at low AO concentrations (up to 5 μM AO). For concentrations of AO over 5 μM, AO fluorescence is increasingly attenuated indicating the formation of bound AO dimers (16–18) and the onset of self-absorption processes in the cuvette. The observed intensity from AO stained cells is ~50% of the intensity observed from the aqueous DNA solutions at each concentration of AO <5 μM.

We conclude from the lack of spectral shifts (Fig. 3) and the linearity of the fluorescence intensity at low AO concentrations (Fig. 4), that below 5 μM, the formation of bound species of AO is small. These results are consistent with those of other researchers (17–19, 28). Similarly, the emission spectral band shapes and maxima of HO stained cells did not depend on the amount of dye

TABLE 1 Spectral properties of aqueous HO and AO nucleic acid complexes

	Absorption		Emission	
HO	abs max	mol abs	em max	Quantum yield
Free dye*	340	36000		0.005
DNA complex*	340	36000	466	0.48
PBLs	¶	¶	454	¶
AO				
Free dye‡				
monomer	492	69000	532	0.40
dimer	466	45700	—	0.01
DNA complex§	498	46000	526	0.88
RNA complex‖	463	—	650	—
PBLs	¶	¶	526	¶

*This work and ref. 20; ‡this work and refs. 13–14, and 17–18; §this work and refs. 16–18; ‖refs. 16–18; and ¶not determined, see text for discussion.

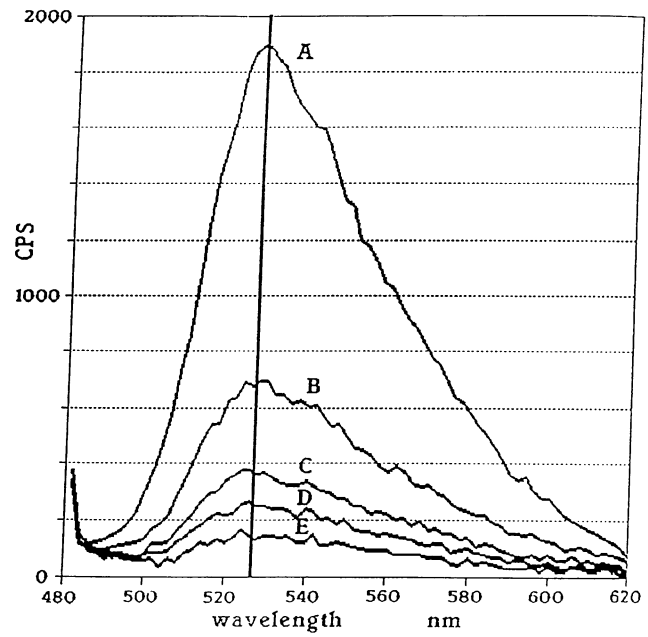

FIGURE 3 Fluorescence emission spectra of AO stained PBLs as a function of AO concentration in the incubating medium. Fluorescence intensity is measured as counts per second (cps) of the PDA detector. The excitation wavelength was 470 nm. The vertical line indicates the position of the emission spectral maximum at 526 nm. The concentrations of AO used where (*A*) 4.82 μM, (*B*) 1.93 μM, (*C*) 0.96 μM, (*D*) 0.64 μM, and (*E*) 0.32 μM.

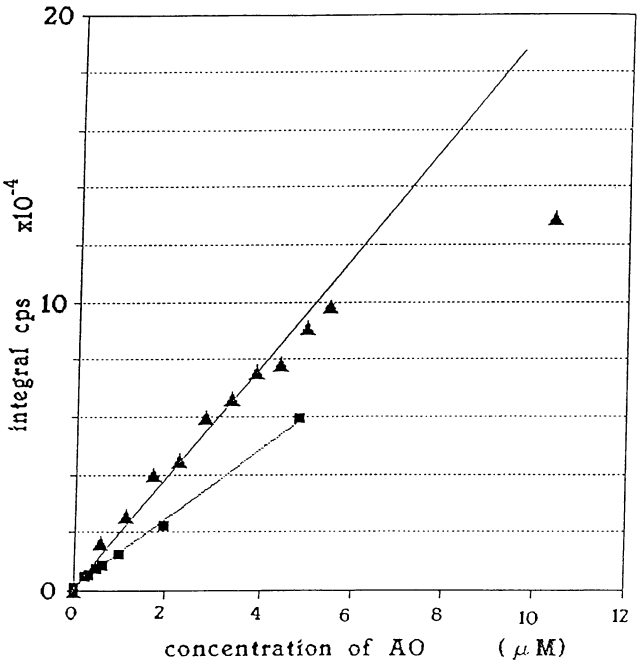

FIGURE 4 Integrated fluorescence intensity as a function of AO concentration in the incubating medium in water saturated with DNA (*triangles*) and PBLs (*squares*). Saturation of the fluorescence signal, indicative of AO dimer formation, begins with AO concentrations above 5 μM (17, 18).

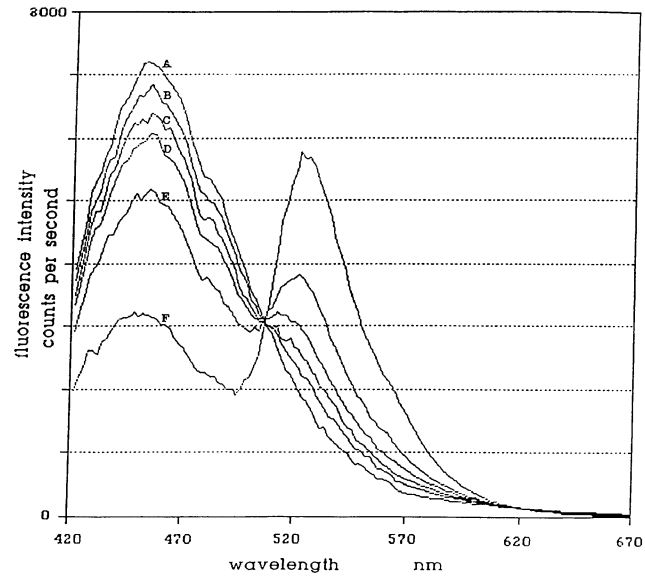

FIGURE 5 Spectral measurement of resonance energy transfer between HO and AO in PBLs. Each curve represents a family of cells stained with equal amounts of HO and varying amounts of AO. The excitation wavelength was 350 nm. The concentrations of AO during incubation were (*A*) none (*B*) 0.32 μM (*C*) 0.64 μM, (*D*) 0.96 μM, (*E*) 1.93 μM, and (*F*) 4.82 μM.

in the incubation medium at the concentrations used in these experiments. The fluorescence quantum distribution functions of HO and AO (measured in PBLs) were used in the calculation of the overlap integral and for the image processing coefficients. Also, the linearity of fluorescence emission with AO concentration indicates that the cells were not saturated with the dye and suggests that the accumulation of AO in cells can be described by concentration diffusion kinetics.

Fig. 5 shows the emission spectra of a family of HO stained cells excited with 350-nm light. Each sample cuvette held 2.4×10^6 stained cells/ml. Curve *A* shows the emission spectrum of cells stained with only HO. The intensity maximum of Curve *A* occurs at 454 nm with weak fluorescence observed at wavelengths >520 nm. Curves *B* through *F* show emission from HO cells after incubation with increasing amounts of AO. As increasing concentrations of AO are used, the emission at wavelengths higher than 520 nm progressively increases, whereas the 454-nm fluorescence is decreased.

The apparent isosbestic points at 507 and 620 nm in Fig. 5 suggest that the presence of only two species suffice to explain the energy transfer. We have not determined whether 620 and 507 nm are true isosbestic points. The HO emission maximum in each of the spectra occurs at 454 nm. At the highest concentration of AO, 55% of the emission from HO is quenched. Although donor quenching would be observed if HO was being displaced from the DNA complex at the high concentrations of AO, the observation of sensitized acceptor fluorescence confirms the occurrence of energy transfer. The consistency of the HO emission band shape further suggests that RET is the predominant energy transfer mechanism. The FWHM of the HO emission (after correcting for overlapping AO emission) is 80, 80, 80, 76, 74, and 72 nm for curves *A*, *B*, *C*, *D*, *E*, and *F*, respectively. Because RET occurs without changing the observed band shape of either the donor or acceptor fluorophores, the amount of trivial energy transfer may be estimated from the amount of narrowing of the donor fluorescence band shape as higher wavelength photons are selectively absorbed by acceptor molecules. The occurrence of energy transfer by the trivial reabsorption mechanism increases with AO concentration as predicted, but RET remains the predominant mechanism.

Table II lists the measured emission anisotropy (r_0) for the dyes bound to DNA in aqueous solution and in PBLs. r_0 was used to calculate axial depolarization

TABLE 2 **Emission anisotropy (EA) data and determination of κ^2 limiting values***

	EA‡	$\langle d_x \rangle$	κ^2	
Aqueous DNA complex			min	max
HO	0.178 ± 0.006	0.67 ± 0.01		
AO	−0.040 ± 0.006	0.32 ± 0.03	0.3	1.7
		−0.32 ± 0.03		
PBLs				
HO	0.160 ± 0.009	0.63 ± 0.02		
AO	−0.12 ± 0.02	0.55 ± 0.05	0.3	2.2

*Refs. 11 and 12; and ‡not corrected for Brownian motion of substrate.

factors ($\langle d_x \rangle$) according to reference 12:

$$\frac{r_0}{0.4} = \langle d_x \rangle^2. \quad (1)$$

The $\langle d_x \rangle$ values were used to determine the limiting values for the energy transfer orientational factor (using Fig. 9 of reference 12). As the viscosity of the nuclear material was unknown, no attempt was made to account for the internal motion of the nuclear or aqueous DNA in the emission anisotropy measurements. The resulting overestimation of the orientational freedom of the bound donor and acceptor stretches the limiting range of κ^2 values. The small emission anisotropy observed for intercalated AO is due to energy transfer between bound AO molecules (29). Time resolved emission anisotropy measurements at very low dye concentrations are required for the establishment of more precise estimates of the fundamental emission anisotropy of the bound dyes (30).

The uptake of AO by PBLs over a 15 min timed interval was followed by observing energy transfer between AO and HO with the low light level imaging apparatus. Fig. 6 shows a series of intensity ratio maps from a single microscope field of six HO saturated cells that were in medium containing AO. Images were captured over a period of 15 min. Only the nuclear regions of the cells are shown in the maps. Images were timed from the point where 4.82 μM AO in PBS was allowed to flow into the 60-μL chamber described above. The cells were excited with 350 nm light. The maps were constructed after calibrating the intensity of each pixel according to Eqs. 5 and 6. The acceptor image was divided by the donor image to obtain the map.

Fig. 6 includes the palette used to color code the AO/HO intensity ratio maps. Table 3 lists the calibrated acceptor/donor intensity ratios that correspond to each color of the palette, and the calculated upper and lower limits of AO-HO average intermolecular separation. In the maps, blue pixels show regions of low AO/HO intensity ratio (high AO-HO separation). Pixels where the AO/HO intensity ratio is near one (the Förster critical distance) are green. Pixels with successively higher AO/HO intensity ratios (closer separations of AO-HO) are represented by yellow, brown, red, purple, and grey. The choice of this sixteen color palette limits the resolution of DNA structure contained in the image data, but facilitates the observance of the stable patterns of AO accumulation in the nucleus.

Image areas where RET occurs are identified by the sensitized emission of acceptor fluorescence and the concurrent quenching of donor fluorescence. Thus, nuclear pixels are easily distinguished from cytoplasmic pixels. Pixels with AO intensity in the acceptor image and no HO intensity in the donor image are necessarily cytoplasmic because HO will only fluoresce when bound to DNA. It is thus, easy to distinguish dye fluorescence from cellular autofluorescence, nonspecifically bound AO, and unbound AO in the ratiometric images. In the cytoplasm, AO fluorescence is excited by the trivial energy transfer process initiated by photons emitted by the fluorochromes bound in the nucleus. Cytoplasmic fluorescence accounts for $<10\%$ of the total observed fluorescence intensity in the images even after 15 min of observation. Only DNA bound AO is close enough to HO to be excited by RET.

Fig. 7 shows the quantitative analysis of the maps of Fig. 6 and two other single field families of PBLs at rest in medium containing AO. The average acceptor/donor intensity ratio for the entire calibrated image is plotted for each field of cells as a function of time for cells in 60 μL of 4.82 μM AO (*solid rectangles*), 0.482 μM AO (*empty rectangles*), and 0.241 μM AO (*triangles*). The dotted horizontal lines show the intensity ratio of the AO and HO fluorescence observed spectrofluorometri-

FIGURE 6 Contour maps of the calibrated AO/HO intensity ratio of the nuclear regions of six cells. The accumulation of AO occurs in spatially distinct regions of the nuclei. Regions of high AO/HO indicate regions of more accessible (less dense) DNA and may correspond to regions of high transcriptional activity. Regions of consistently low AO/HO correspond to areas of high heterochromatin content. The cells shown were all part of a single, typical microscope field that was chosen at random. The field was ~80 μm in diameter. The average diameter of a human PBL is 10 μm, the nuclei shown here average 7 μm in diameter. (0 s) No AO intensity observed. (65 s; *B*) A small area appears where the AO-HO separation already approaches the Förster critical distance. (126 s; *A, C–F*) Emerging patterns of AO accumulation. (*B*) Area of high AO/HO intensity has expanded. (186 s; *A*) Regions of high AO/HO (present after 65 s) emerge. (*E*) AO accumulation is slow. (338 s; *A*) High intensity spot near the center of the map. (*B*) Emergence of a second high intensity region. (*C*) Emergence of a pattern of AO accumulation. (427–666 s; *E* and *F*) AO accumulation occurs throughout with the emergence of a distinct pattern that spans the nucleus. (907 s) In some regions there is a decrease in AO/HO intensity ratio. See text for discussion.

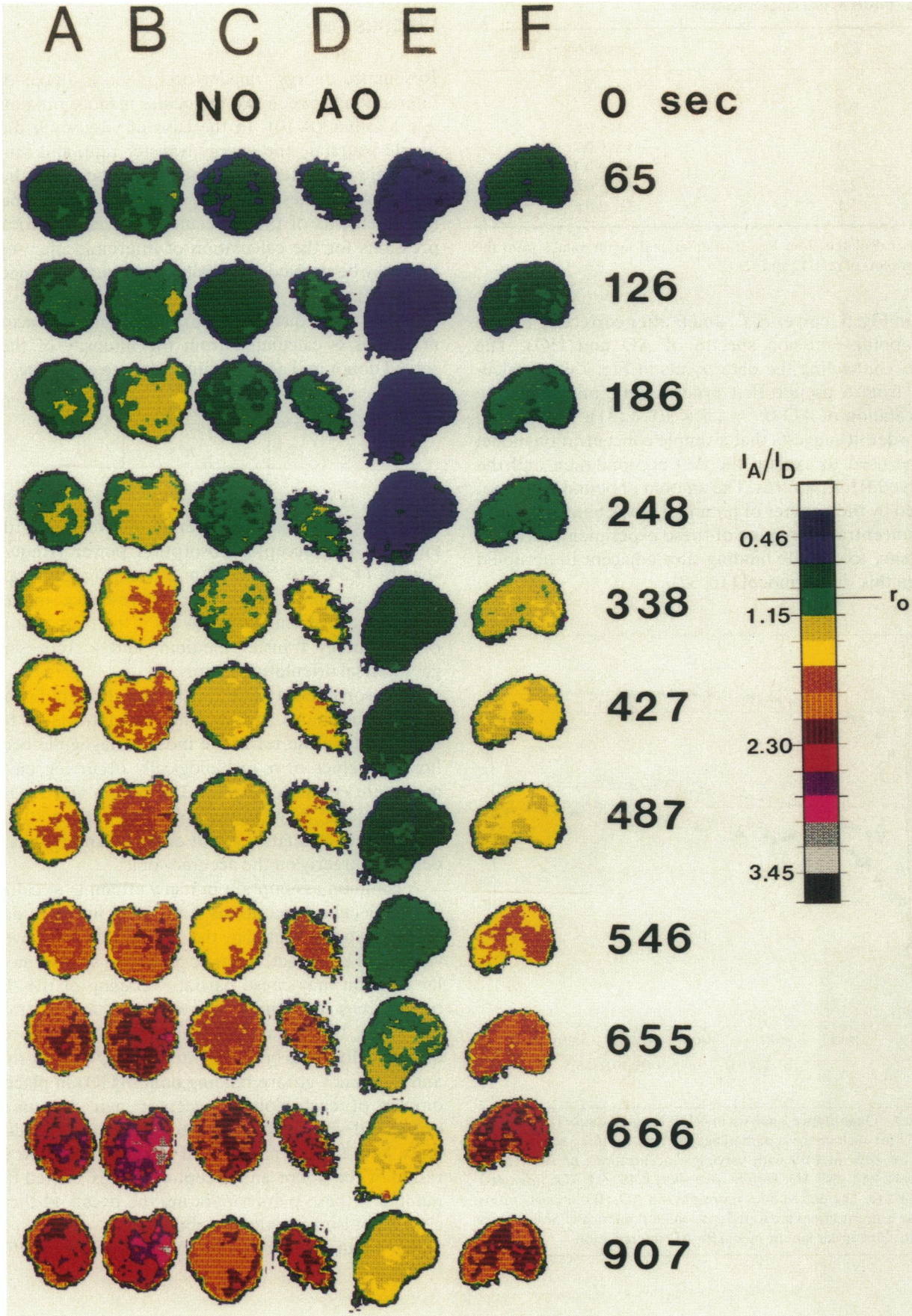
A B C D E F
NO AO
0 sec
65
126
186
248
338
427
487
546
655
666
907
I_A/I_D
0.46
1.15
r_o
2.30
3.45

TABLE 3 **Proximity and range calculations***

I_A/I_D	Separation
	(nm)
0.00	∞
0.46	5.1 ± 0.8
1.00	4.5 ± 0.7
1.15	4.4 ± 0.7
2.30	3.9 ± 0.6
3.45	3.6 ± 0.6

*Limits calculated from Eq. 2; orientational factor values from the contour plots of refs. 11 and 12.

cally in Fig. 5 (curves *F*, *C*, and *B* after correcting for the overlapping emission spectra of AO and HO). The curves connecting the data points in Fig. 7 were calculated from a pseudo first order kinetic model for the intercalation of AO ($k = 1.7 \times 10^{-3}$) (31). The pseudo first order fit suggests that a simple concentration model can be used to explain the AO accumulation and the observed RET patterns. The amount of bound AO is not limited by the number of potential DNA binding sites in the concentration regime of these experiments, nor is it necessary to exclude binding sites adjacent to occupied sites in this simple model (16, 32).

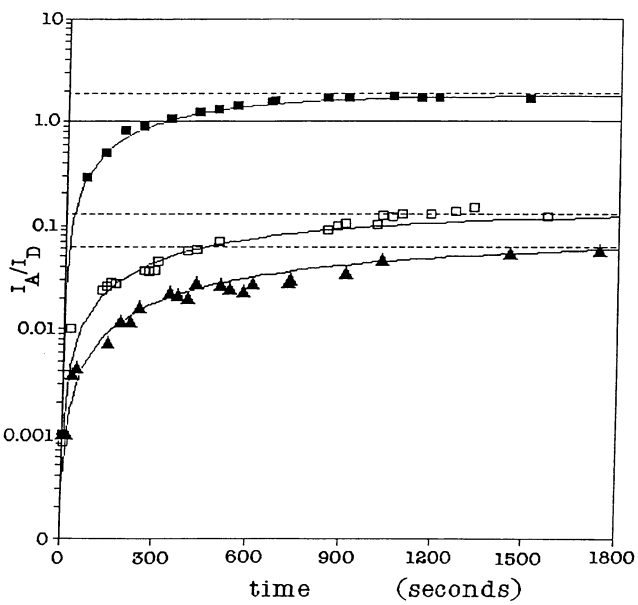

FIGURE 7 Quantitative analysis of RET imaging data. The average AO/HO for each image is plotted against time for three sequences of images of cells in PBS with varying concentrations of AO. (*Solid rectangles*) 4.82 μM AO; (*empty rectangles*) 0.48 μM AO; (*triangles*) 0.24 μM AO. The dotted lines represent the AO/HO intensity ratios for these concentrations measured spectrofluorometrically. Solid curves are fit to a first order kinetic model for AO intercalation.

DISCUSSION

Resonance energy transfer occurs via a dipole–dipole interaction between two molecules in close proximity to one another (8–10). In the case of very weak dipole–dipole coupling, the energy transfer rate, and thus the separation between and relative orientation of the two transition dipoles, may be calculated from spectral measurements of the molecules involved. Identical expressions for the calculation of intermolecular separation may be derived classically or via quantum mechanics (8–10).

The average distance separating donor and acceptor molecules is calculated from the intensity of the observed donor and acceptor fluorescence emissions:

$$r = \left[\frac{7.096 \times 10^{14}\kappa^2 q_D O}{\frac{I_A}{I_D} n^4}\right]^{1/6}, \quad (2)$$

where q_D is the quantum efficiency of the donor molecule, O is the spectral overlap between the donor emission and acceptor absorption power (frequency) spectra (1.34×10^{-52} cm^2 s^4/mol from Fig. 2), I_A and I_D are the acceptor and donor fluorescence intensities (calibrated as discussed below), n is the refractive index of the energy transfer medium, and κ^2 represents a geometrical orientation factor.

A reasonable estimate for the refractive index of the nuclear material is 1.5 (33). The error introduced by the uncertainty in the refractive index is negligible because limiting values of n in biologically occurring environments are certainly between 1.3 (water) and 2. On the other hand, κ^2 may assume any value between 0 and 4. The correct evaluation of all energy transfer data thus depends largerly on the accuracy of κ^2.

A common assumption in many attempts to calculate intermolecular separations from RET intensity data is that κ^2 is approximated by the isotropic dynamic average value ⅔ (11). In fact, dynamic processes such as molecular rotation may cause partial averaging of the dipole orientations on a time scale shorter than the transfer time (12). In the case of the DNA probes, where the double helix holds both the intercalating acceptor (AO) and the minor groove binding donor (HO) in place, the dipoles of each donor/ acceptor pair are uniquely orientated with respect to each other. In the double helix, both the orientation and the intermolecular separation of the donor and acceptor dipoles is fixed by the number of base pairs separating the dyes and they are clearly not isotropically distributed.

Fig. 8 illustrates the minor groove binding of HO and

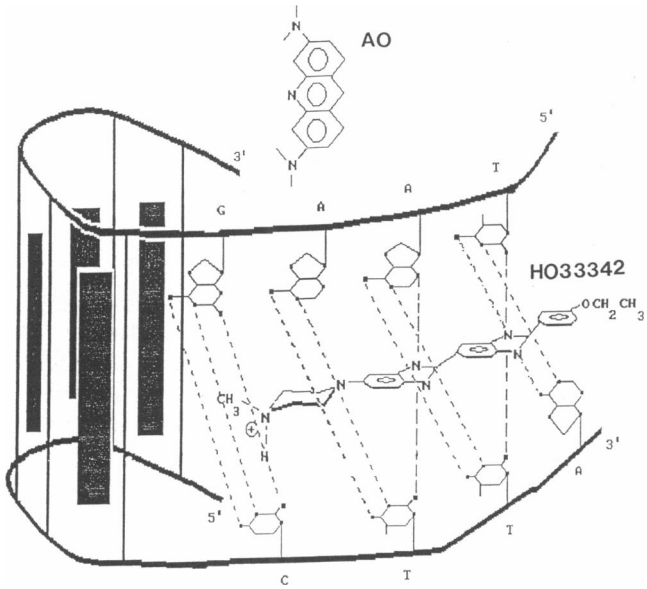

FIGURE 8 Depiction of minor groove binding of HO and intercalation of AO. AO intercalation may be to any of the four sites shown by rectangles. Each intercalation site shown has a specific molecular environment due to the local nucleic acid base pair sequence and proximity to HO. The AO-HO intermolecular separation and relative orientation depend on the occupied intercalation site. The intermolecular distances calculated here thus represent the average regional HO/AO separation.

intercalation of AO (22, 23). AO intercalation may be between any two base pairs. Four possible intercalation sites are shown by the shaded rectangles in Fig. 8. Because the emission transition moment for HO and the absorption transition moment of AO lie in their respective molecular planes, the dipoles will be nearly perpendicular when separated by one or two base pairs. As the molecular distance increases, a more favorable orientation for energy transfer between HO and AO develops. Consequently, the energy transfer efficiency is not a monotonically decreasing function of intermolecular separation. The orientation of AO/HO is restricted by the helical structure of the nucleic acid and the use of $\frac{2}{3}$ for κ^2 is clearly inappropriate.

The accuracy of the estimation of κ^2 is, thus, the limiting factor in calculating intermolecular separations from RET intensity data. For the case of excitation to the lowest lying excited state of donor, the orientational freedom of the donor and acceptor dipoles and their relative orientation can be clarified with polarization spectroscopy. Numerical relationships between observed emission anisotropies of the fluorophores in solution, the transfer depolarization, and the orientation factor limits have been derived by Dale et al (11). The maximum and minimum values for the orientation factor used here were obtained from their contour plots of donor and acceptor axial depolarization factors. More precise determinations of the spatial distribution of geometric orientations in the images (by the measurement of the decay of emission anisotropy) were prohibited in the images by relatively slow recovery time of the image intensifier.

The occurrence of RET itself will not perturb the emission bandshape of the donor or the absorption spectrum of the acceptor molecule (2). Therefore, in the absence of competing physical processes, photochemistry, self-absorption, and autofluorescence, the amount of observed RET in the images can be calculated from the amount of observed fluorescence at the donor and acceptor emission wavelengths. The quantum distribution functions of the dyes, the transmission spectra of the emission filters, and the spectral sensitivity of the primary imaging component (the intensifier in these experiments) are used to find the contributions to observed intensity made by each dye. The calibration procedure is limited at high concentrations of acceptor dye. Self-absorption and trivial energy transfer cause the observed emission spectra to deviate from the quantum distribution functions of the dyes because the lowest frequencies of donor emission are absorbed in the presence of acceptor (Fig. 5). Similarly, acceptor–acceptor or donor–donor self absorption may occur with attendant distortions in the observed spectra and are expected to be increasingly important at high dye concentrations.

The observed fluorescence intensity though an emission barrier filter has components originating from both the energy donor and energy acceptor:

$$I_1 = \int S(\lambda)T_1(\lambda)[I_A f_A(\lambda) + I_D f_D(\lambda)]\, d\lambda \qquad (3)$$

$$I_2 = \int S(\lambda)T_2(\lambda)[I_A f_A(\lambda) + I_D f_D(\lambda)]\, d\lambda, \qquad (4)$$

where $T_1(\lambda)$ and $T_2(\lambda)$ are the transmission spectra of the donor (Eq. 3) and acceptor (Eq. 4) barrier filters, and $f_D(\lambda)$ and $f_A(\lambda)$ are the quantum distribution functions of the donor (D) and acceptor (A) dyes as a function of emission wavelength. $S(\lambda)$ is the spectral response of the primary imaging component. $T_1(\lambda)$, $T_2(\lambda)$, $f_D(\lambda)$, $f_A(\lambda)$, and $S(\lambda)$ are measured independently.

Eqs. 3 and 4 can be expressed as two equations in two unknowns with constant coefficients R_n^X as defined in Table 4. For the calculation of the coefficients, the integrals shown in Table 4 are replaced by sums over the transmission band pass of each filter. The fluorescence intensity attributed to emission from the donor (I_D) or acceptor (I_A) dye is calculated in each image on a pixel

TABLE 4 **Image processing coefficients for HO and AO**

Integral	Symbol	Value
$\int S(\lambda)T_1(\lambda)f_D(\lambda)d\lambda$	R_1^D	0.135
$\int S(\lambda)T_1(\lambda)f_A(\lambda)d\lambda$	R_1^A	0.0
$\int S(\lambda)T_2(\lambda)f_D(\lambda)d\lambda$	R_2^D	0.037
$\int S(\lambda)T_2(\lambda)f_A(\lambda)d\lambda$	R_2^A	0.280

by pixel basis by solving Eqs. 3 and 4:

$$I_D = \frac{R_2^A I_1 - R_1^A I_2}{R_1^D R_2^A - R_2^D R_1^D} \quad (5)$$

$$I_A = \frac{R_1^D I_2 - R_2^D I_1}{R_1^D R_2^A - R_2^D R_1^A}, \quad (6)$$

where R_n^X is the coefficient for probe X through the n emission barrier filter (defined as $R_n^X = \int S(\lambda)T_n \cdot (\lambda)f_X(\lambda)\,d\lambda$). Obviously, it is necessary to calculate new coefficients for different combinations of transmission filters and/or staining fluorochromes.

RET imaging permits the direct observation of the distribution of chromatin density in the interphase nucleus. We postulate that because of its decreased density, euchromatin has greater accessibility to the intercalating AO than the more dense heterochromatin (34). In the calibrated images, regions high in euchromatin content correspond to areas of high acceptor/donor intensity ratio. The accumulation of AO occurs in distinct zones following stable patterns in the nuclei. The patterns observed in the nuclei are analogous to the two-phase patterns observed after staining of nuclear chromatin in electron micrographs (35).

Regions of high AO/HO intensity appear near the nuclear/cytoplasmic border of each of the nuclei, but are clearly within the border of the nucleus. We were unable to determine whether some or all of the initially bright areas are directly attached to the nuclear/cytoplasmic border in these two-dimensional images. Regions of consistently low AO/HO ratio also occur in each of the nuclei. In addition, and more importantly, at no time before 15 min do any pixels decrease in AO/HO intensity ratio in the 0 to 666 timed period. Because only the DNA bound AO is close enough to HO to participate in RET, the lack of decreasing pixels supports our suggestions that the AO binds irreversibly in nuclear regions of high affinity and that RET is the predominant mechansim of energy transfer.

The observation of nuclear structure in the images is ultimately limited by the amount of AO uptake for three reasons. (*a*) Each intercalated AO causes a 10° local unwinding of the DNA helix and slightly increases the separation between two adjacent base pairs (19). This local stretching of the DNA increases the intermolecular separation of the minor groove bound HO and causes an overall decrease in AO/HO intensity ratio. (*b*) The overlap integral of acceptor–acceptor energy transfer (AO emission coupled with AO absorption) is 6.13×10^{-53} cm^2 s^4/mol compared to 1.34×10^{-52} cm^2 s^4/mol for acceptor-donor RET. Despite the local stretching described above, as the accumulation of AO increases, the average distance between AO molecules decreases, and the occurrence of acceptor–acceptor RET increases. The initiation of AO singlet–singlet exciton annihilation processes would cause a decrease in observed AO emission intensity. (*c*) The increased likelihood of trivial RET and homogeneous RET as the amount of AO bound to biological molecules other than β-DNA increases. The buildup of AO in the cytoplasm acts as a filter to attenuate the observed high wavelength emission.

The combination of DNA stretching, increases in nonspecific AO binding, and the initiation of self transfer contribute to the decrease in AO/HO intensity ratio observed at 907 s in Fig. 6.

Limitations of RET imaging

The need to remove background intensity potentially limits quantitative RET measurements. Three primary components of background noise in these measurements are camera dark current, nonuniform illumination and cellular autofluorescence. The KS-1381 image intensifier and CCD camera combination was used to insure linear amplification of the input fluorescence intensity at low light levels throughout the image field, and a low uniform dark current. For the calculations of acceptor/donor intensity ratio of Figs. 6 and 7, we assumed that the fluorescence intensity from the cells was additively superimposed onto the background at the fixed illumination power levels. From the analysis of the grey level histograms of background images, we estimate that the contribution of stray light is approximately 18% of the thermal noise. Thus, from the sixth root dependence of the intermolecular calculation on the acceptor/donor intensity ratio, the assumption of background additivity contributed no more than 7% error in the lowest signal to noise images.

Contributions from intrinsic cellular fluorescence (autofluorescence) are not removed by the subtraction of dark current. It is difficult to remove autofluorescence contributions in imaging experiments because of its spatial distribution (40). In the approach presented here, the removal of autofluorescence would require the addition of spatial terms in Eqs. 3 and 4 and measuring images of the unstained cells at the wavelengths of both the donor and acceptor dyes. Such measurements are not usually possible. Alternatively, autofluorescence

contributions may be approximated by measuring the fluorescence spectrum of unstained cells. These spectra are typically broad and featureless so that intrinsic fluorescence at the acceptor wavelength cancels the intrinsic fluorescence at the donor wavelength during image ratioing. Intrinsic fluorescence in the visible spectral region arises primarily from intracellular NADH, riboflavin, flavin coenzymes, and flavoproteins bound in the mitochondria (40). Therefore, the nuclear maps shown in Fig. 6 should contain only small contributions from fluorescence other than the probes.

Accuracy in the determination of the orientational factor is the largest source of uncertainty in these measurements. As discussed above, simple substitution of ⅔ as the average value for κ^2 is clearly inappropriate for the case of DNA binding dyes. The range of possible orientational values must be established to evaluate the uncertainty in the calculation of average intermolecular separation. The steady-state emission anisotropy measurements used here do not separate the motion of the dye from that of the DNA itself. The range of limiting values of κ^2 is therefore overestimated in this study (11, 12). The wide range of values leads to an uncertainty of ~20% in the calculation of average intermolecular separations and in the calculated value of the Förster critical distance. The uncertainty in the calculated values also increases as the actual intermolecular separation decreases. Time resolved measurements of emission anisotropy decay or cryogenic studies of the DNA bound dyes would more precisely establish the orientational freedom of dyes and permit more accurate determinations of the range of κ^2 values.

Low incident power fluxes (80 $\mu W/cm^2$ at 350 nm) were used to minimize photobleaching and dye saturation. Our results show that AO is more sensitive to photobleaching than HO. The first order rate constant for photobleaching of HO is $<0.001\ s^{-1}$. Previously reported measurements of AO photobleaching rate constants range from 0.048–0.15 s^{-1} (36). The maps were constructed from images that are averages of 60 images taken over a 1 s period. We therefore estimate the uncertainty in the AO/HO intensity ratio due to photobleaching to be between 5–14%. Thus, from the sixth root dependence of the Förster critical distance on the intensity ratio, photobleaching contributes at most 2.5% uncertainty in the calculation of intermolecular distances.

Self transfer processes also limit the resolution of nuclear substructure at high dye concentration. As shown in Fig. 6 and Table 3, as AO accumulates the average distance between acceptor molecules and donor molecules decreases. The increased proximity will lead to the establishment of energy migration networks within the nucleus. As the excited state is passed from molecule to molecule, the probabilities of thermal relaxation and singlet–singlet exciton annihilation increase.

In these experiments, the occurrence of self absorption and energy migration processes may be evaluated as follows. The acceptor-donor overlap integral is $1.34 \times 10^{-52}\ cm^2\ s^4/mol$. In comparison, the overlap integral for donor–donor transfer (donor absorption with donor emission) is $1.10 \times 10^{-54}\ cm^2\ s^4/mol$ whereas the overlap integral for acceptor–acceptor transfer is $6.13 \times 10^{-53}\ cm^2\ s^4/mol$. For identical intermolecular separations and orientational factors (i.e., based on the magnitude of the overlap integrals alone) the probability of acceptor–acceptor transfer processes is 45.7% of acceptor-donor processes. Donor–donor energy transfer is negligible. However, as increasing amounts of AO accumulate in the cells acceptor–acceptor self transfer assumes an important role and quantitative evaluations of donor-acceptor intermolecular distances by RET are more difficult (Fig. 6; 907 s).

Finally, the binding of fluorescent probes certainly changes the native conformational structure of the nucleic acid. Intercalating dyes such as AO and ethidium bromide may cause either local unwinding or winding by the DNA helix (19, 37). The degree to which the incorporation of various dyes change normal cellular structure and function must be evaluated. These interactions ultimately limit the utility of fluorescence labeling techniques, including RET imaging.

CONCLUSION

In this paper, we have shown a calibration procedure for the acquisition and quantitative analysis of resonance energy transfer image data. The occurrence of energy transfer between two DNA dyes, HO and AO was characterized by low concentration spectral measurements. The critical distance for energy transfer for these two dyes, measured in an environment closely approximating their in situ environment, is 4.5 ± 0.7 nm. The first quantitative high resolution RET images were presented, revealing the nuclear structure in six human peripheral blood leukocyte nuclei.

The calibrated RET images provide a means of spatially distinguishing nuclear regions of eu- and heterochromatin. The temporal accumulation of submicromolar quantities of AO over a period of 15 min was measured. In contrast to flow cytometric techniques, a single field containing six cells was continuously observed. Changes in calibrated intensity ratios are sensitive to changes in distance on the order of a few nanometers, and thus reveal low level nuclear structure. Although the individual chromatin strands themselves were not resolved, its dispersal throughout the nucleus

(usually undetectable in optical or elecron microscopy) is seen as patterns of increasing acceptor to donor intensity ratio. Interphase chromosomes are known to be associated with the nuclear lamina, with the centromeres and telomeres located at opposite cellular poles (35, 38, 39). In Fig. 6, the majority of the brightly occurring spots are found along the edges of the maps. Spots located in the center of these maps may also be associated with the nuclear lamina, but this association is not clearly seen in these two dimensional images.

While the structural and molecular basis of interactions between the nuclear matrix and interphase chromatin are not well understood, the dispersal of chromatin in the interphase nucleus is nonrandom and clearly essential for the transcription and replication of DNA (34, 35, 38, 39). The combined use of optical sectioning (confocal) microscopy and RET imaging techniques should further elucidate the three dimensional structural order of interphase chromosomes. The vast assortment of biologically specific and commercially available dyes makes RET imaging a promising technique for high resolution structural studies of other cellular components.

The authors are grateful to Dr. Louis D. Homer and Dr. Taffy Williams for their insightful and valuable commentary. We also thank Dr. Steven Yeandel and Art Shaeffer for their extremely helpful comments, advice, and suggestions. Views presented in this paper are those of the authors: no endorsement by the Department of the Navy has been given or should be inferred.

This work was completed under Naval Medical Research and Development Command work unit No. MR00001.001-1382. Michael Ludwig held a National Research Council-Naval Medical Research Institute Research Associateship.

Received for publication 28 January 1991 and in final form 25 November 1991.

REFERENCES

1. Fluorescence Microscopy of Living Cells in Culture, Methods Cell Biology; Vols 29 and 30. 1989. Taylor, D. L. and Wang, Y. L. Academic Press, San Diego, 503 pp.
2. Herman, B. 1989. Resonance energy transfer microscopy. *In* Methods in Cell Biology, Vol. 30. D. L. Taylor and Y. L. Wang, editors. Academic Press, San Diego. 220–243.
3. Stryer, L., and R. P. Haugland. 1967. Energy transfer: a spectroscopic ruler. *Proc. Natl. Acad. Sci. USA.* 58:719–726.
4. Inoue, S. 1987. Video Microscopy. Plenum Publishing Corp., New York.
5. Agard, D. A., and J. W. Sedat. 1983. Three-dimensional architecture of a polytene nucleus. *Nature (Lond.).* 302:676–681.
6. Arndt-Jovin, D. J., M. Robert-Nicoud, and T. M. Jovin. Probing DNA structure and function with a multi-wavelength fluorescence confocal laser microscope. 1990. *J. Microsc.* 157:61–72.
7. Haugland, R. P. 1989. Molecular Probes Handbook of Fluorescent Probes and Research Chemicals. Molecular Probes, Inc. Eugene, OR. 234 pp.
8. Förster, Th. 1964. Delocalized excitation and excitation transfer. *In* Modern Quantum Chemistry, Vol 3. O. Sinanoglu, editor. Academic Press, New York. 93–137.
9. Kuhn, H. 1982. Energy transfer mechanisms. *In* Biophysics. W. Hoppe, W. Lohmann, H. Markl, and H. Ziegler, editors. Springer Verlag, Berlin. 279–288.
10. Stratton, J. A. 1941. Electromagnetic Theory. McGraw-Hill Book Co. 615 pp.
11. Dale, R. E., J. Eisinger, and W. E. Blumberg. 1989. The orientational freedom of molecular probes. *Biophys. J.* 26:161–193.
12. Dale, R. E., and J. Eisinger. 1975. Polarized excitation energy transfer. *In* Biochemical Fluorescence: Concepts, Vol. 1. R. F. Chen and H. Edelhoch, editors. Marcel Dekker, New York. 115–284.
13. Armstrong, R. W., T. Kurucsev, and U. P. Strauss. 1970. The interaction between acridine dyes and deoxyribonucleic acid. *J. Am. Chem. Soc.* 92:3174–3181.
14. Muller, W., and F. Gautier. 1975. Interactions of heteroaromatic compounds with nucleic acids A-T. Specific non-intercalating DNA ligands. *Eur. J. Biochem.* 54:385–394.
15. Peacocke, A. R., and J. N. H. Skerrett. 1956. The Interaction of Aminoacridines with Nucleic Acids. *Trans. Farad. Soc.* 52:261–279.
16. Rigler, R. 1966. Microfluorometric Characterization of Intracellular Nucleic Acids and Nucleoproteins by Acridine Orange. *Acta Physiol. Scand.* 67:Supplementum 267:1–122.
17. Kapuscinski, J., and Z. Darzynkiewicz. 1987. Interactions of acridine orange with double stranded nucleic acids. Spectral and affinity studies. *J. Biomol. Struct. Dynam.* 5:127–143.
18. Beers, R. F., D. D. Hendley, and R. F. Steiner. 1958. Inhibition and activation of polynucleotide phosphorylase through the formation of complexes between acridine orange and polynucleotides. *Nature (Lond.).* 182:242–244.
19. Darzynkiewicz, Z., F. Traganos, J. Kapuscinski, L. Staiano-Coico, and M. R. Melamed. 1984. Accessibility of DNA in situ to various fluorochromes: relationship to chromatin changes during erythroid differentiation of friend leukemia cells. *Cytometry.* 5:355–363.
20. Latt, S. A., and G. Stetten. 1976. Spectral Studies on 333258 Hoechst and related bisbenzimindazole dyes useful for fluorescent detection of deoxyribonucleic acid synthesis. *J. Histochem. Cytochem.* 24:24–33.
21. Arndt-Jovin, D. J., and T. M. Jovin. 1977. Analysis and sorting of living cells according to deoxyribonucleic acid content. *J. Histochem. Cytochem.* 25:585–589.
22. Pjura, P. E., K. Grzeskowiak, and R. E. Dickerson. 1987. Binding of Hoechst 33258 to the minor groove of β-DNA. *J. Mol. Biol.* 197:257–271.
23. Zimmer, C., and U. Wahnert. 1986. Nonintercalating DNA-binding ligands: specificity of the interaction and their use as tools in biophysical, biochemical, and biological investigations of the genetic material. *Prog. Biophys. Molec. Biol.* 47:31–112.
24. Lalande, M. E., V. Ling, and R. G. Miller. 1981. Hoechst 33342 dye uptake as a probe of membrane permeability changes in mammalian cells. *Proc. Natl. Acad. Sci. USA.* 78:363–367.
25. Boyum, A. 1977. Separation of lymphocytes, lymphocyte subgroups, and monocytes: a review. *Lymphology.* 10:71–76.

26. Gonzalez, R. C., and P. Wintz. 1987. Digital Image Processing. Addison-Wesley, Publishing Company, Reading, MA. 350 pp.

27. Fredericq, E., A. Oth, and F. Fontaine. 1961. The ultraviolet spectrum of deoxyribonucleic acids and their constituents. *J. Mol. Biol.* 3:11–17.

28. Traganos, F., Z. Darzynkiewicz, T. Sharpless, M. Melemed. 1977. Simultaneous staining of ribonucleic acids in unfixed cells using acridine orange in a flow system. *J. Histochem. Cytochem.* 25:46–56.

29. Beisker, W., and W. G. Eisert. 1989. Denaturization and condensation of intracellular nucleic acids monitored by fluorescence depolarization of intercalating dyes in individual cells. *J. Histochem. and Cytochem.* 37:1699–1704.

30. Dix, J. A., and A. S. Verkman. 1990. Mapping of fluorescence anisotropy in living cells by ratio imaging. *Biophys. J.* 57:231–240.

31. Markovits, J., C. Garbay-Jaureguiberry, B. P. Roques, and J. B. Le Pecq. 1989. Acridine dimers: influence of the intercalating ring of the linking-chain nature on the equilibrium and kinetic DNA-binding parameters. *Eur. J. Biochem.* 180:359–366.

32. Nicolini, C., A. Belmont, S. Parodi, S. Lessin, and S. Abraham. 1979. Mass action and acridine orange staining: static and flow cytometry. *J. Histochem. Cytochem.* 27:102–113.

33. Cohen, G., and H. K. Eisenberg. 1968. Deoxyribonucleate solutions: sedimentation in a density gradient, partial volumes, density and refractive index increments, and preferential interactions. *Biopolymers.* 6:1077–1100.

34. Yaniv, M., and S. Cereghini. 1986. Structure of transcriptionally active chromatin. *CRC Crit. Rev. Biochem.* 21:1–26.

35. Davies, H. G., A. B. Murray, and M. E. Walmsley. 1974. Electron-microscope observations on the organization of the nucleus in chicken erythrocytes and a superunit thread hypothesis for chromosome structure. *J. Cell Sci.* 16:261–299.

36. Benson, D. M., J. Bryan, A. L. Plant, A. M. Gotto, and L. C. Smith. 1985. Digital imaging fluorescence microscopy: spatial heterogeneity of photobleaching rate constants in individual cells. *J. Cell Biol.* 100:1309–1323.

37. Paoletti, J., and J. B. Le Pecq. 1971. Resonance Energy Transfer between ethidium bromide molecules bound to nucleic acids. *J. Mol. Biol.* 59:43–62.

38. Igo-Kemenes, T., W. Horz, and H. G. Zachau. 1982. Chromatin. *Annu. Rev. Biochem.* 51:89–121.

39. Gerace, L., and B. Burke. 1988. Functional organization of the nuclear envelope. *Annu. Rev. Cell Biol.* 4:335–374.

40. Aubin, J. E. 1979. Autofluorescence of viable cultured mammalian cells. *J. Histochem. and Cytochem.* 27:36–43.